Fuel 211 (2018) 159–172

Contents lists available at ScienceDirect

Fuel

journal homepage: www.elsevier.com/locate/fuel

Full Length Article

Molecular simulation of adsorption behaviors of methane, carbon dioxide and their mixtures on kerogen: Effect of kerogen maturity and moisture content

Liang Huang[a,b,*], Zhengfu Ning[a,b], Qing Wang[a,b], Rongrong Qi[a,b], Yan Zeng[a,b], Huibo Qin[c], Hongtao Ye[a,b], Wentong Zhang[a,b]

[a] State Key Laboratory of Petroleum Resources and Prospecting, China University of Petroleum (Beijing), Beijing 102249, PR China
[b] Department of Petroleum Engineering, China University of Petroleum (Beijing), Beijing 102249, PR China
[c] State Key Laboratory of Heavy Oil Processing, China University of Petroleum (Beijing), Beijing 102249, PR China

ARTICLE INFO

Keywords:
CH_4 adsorption
CO_2 adsorption
Adsorption selectivity
Kerogen maturity
Moisture content
Molecular simulation

ABSTRACT

The adsorption behaviors of methane (CH_4), carbon dioxide (CO_2) and their mixtures are vital to understand the process of CO_2 sequestration and shale gas exploitation. In this work, four realistic kerogen models with different maturities (immature (IIA), beginning of oil window (IIB), middle of oil window (IIC), postmature (IID)) were built by the molecular dynamics (MD) method. The adsorption characteristics of CH_4, CO_2 and their mixtures on these kerogen models with various moisture contents (0, 0.7, 1.4, 2.1, 2.8 wt%) were investigated by the grand canonical Monte Carlo (GCMC) simulations. The influences of kerogen maturity and moisture content on the adsorption capacity, isosteric heat of adsorption and adsorption selectivity of gas molecules were discussed. Simulation results show that the maximum adsorption capacity of gas molecules increases with increasing kerogen maturity, but decreases with increasing moisture content, and the reduction decreases as the maturity increases at high moisture contents. The average isosteric heat of CO_2 adsorption is relevant to the sulfur/oxygen content of kerogen models. The pre-adsorbed water (H_2O) has a small effect on the gas isosteric adsorption heat when located in the middle of pores, but can reduce the CO_2 isosteric adsorption heat by occupying the hydrophilic groups. Moreover, H_2O molecules are observed to migrate and aggregate into growing clusters at higher moisture contents for kerogen IIC and IID models, increasing the gas isosteric adsorption heat. The CO_2/CH_4 adsorption selectivity gradually decreases to the equilibrium value with the rise of bulk pressure. Also, the selectivity decreases with increasing CO_2 mole fraction for lower mature kerogen models (IIA and IIB), but increases with the CO_2 mole fraction at low pressure for kerogen models of higher maturity (IIC and IID). Meanwhile, the selectivity increases for IIA, IIC and IID models, while decreases for IIB model as the moisture content increases. This study gains deep insights into the effect of kerogen maturity and moisture content on the interaction between CH_4/CO_2 and kerogen at microscopic scale.

1. Introduction

As one of the most promising alternatives to conventional gas resources, shale gas has attracted enormous attentions worldwide for its considerable abundance and high utilization efficiency [1,2]. However, the tight shale reservoir and the complex gas transport mechanisms, along with the natural depletion development regime, result in a low recovery of shale gas reservoirs. Thus the enhancement of gas recovery becomes the key topic for the development of shale gas reservoirs. Injection of CO_2 into coal seams has been proved to be one effective strategy for recovery enhancement of coalbed methane as well as CO_2 sequestration in the past decades [3–5]. This strategy has recently received increasing attentions as one potential technique for CO_2 storage with the potential for enhanced shale gas recovery [6–8]. To further understand this process, a detailed understanding of the adsorption characteristics of shale with CH_4, CO_2 and their mixtures is essential.

The adsorption characteristics of organic matter under reservoir conditions are associated with many factors such as the total carbon content (TOC), kerogen type and maturity, surface functional group, as well as the temperature and moisture content [9]. Of these factors, moisture content acts as one of the most key roles in gas adsorption [10–12]. Clay mineral in shale is widely accepted as water-wet, while

* Corresponding author at: State Key Laboratory of Petroleum Resources and Prospecting, China University of Petroleum (Beijing), Beijing 102249, PR China.
E-mail address: huangliang19911015@163.com (L. Huang).

http://dx.doi.org/10.1016/j.fuel.2017.09.060
Received 2 April 2017; Received in revised form 20 August 2017; Accepted 14 September 2017
Available online 21 September 2017

organic matter is traditionally assumed as hydrocarbon-wet [13]. However, experimental and simulation work recently found that kerogen is actually mixed-wet due to the hydrophilic characteristic of oxygen-bearing groups [14]. Shale in the reservoir is originally at moisture equilibrated conditions [15]. H_2O molecules can not only block the throats of shale, but also occupy the adsorption sites for gas molecules, thus rapidly reducing the adsorption capacity [16–17]. Another significant parameter relevant to gas adsorption is the maturity of organic matter in shale. Almost half of the total hydrocarbons in shale are adsorbed in the organic matter for its abundant adsorption sites [18]. The organic matter maturity is closely correlated with the surface functional groups and micropore volumes, which directly determine the gas adsorption capacity [19]. Therefore, the influence of moisture content and maturity on adsorption characteristics of shale should be emphasized and discussed in detail.

To date, some experimental attempts have been made to investigate the adsorption characteristics of organic materials considering the influence of maturity and moisture content. Gas adsorption capacity has been observed to be reduced significantly with the equilibrated moisture in shale and coal [19,20]. Meanwhile, adsorption capacity of shale gas has been found to be linearly correlated with the maturity [21–23]. Particularly, it increases as the maturity increases [21]. Gensterblum et al. [10] experimentally investigated the competitive adsorption of CH_4 and CO_2 on organic material in the presence of moisture. Gensterblum et al. [24] studied the effect of coal rank and moisture content on CH_4 and CO_2 adsorption on natural coals. Experimental investigation is the fundamental method for understanding gas adsorption process [25]. Also, experimental data are important reference resources for evaluating the validity of molecular models. The development of molecular simulation provides an effective tool for predicting adsorption performances of gas molecules in complex systems at molecular scale [26,27], which is complemental to the experimental study. Encouraging results for studies on gas adsorption behaviors with molecular simulation techniques have been reported [27–29]. Zhang et al. [27] investigated the adsorption characteristics of CH_4 on dry and moist coal with the combined Monte Carlo and MD simulations. Liu et al. [28] studied the influence of moisture content on the adsorption behaviors of pure CH_4, CO_2, N_2 molecules and their mixed gases on coal models with heterogeneous surface through GCMC simulations. Zhao et al. [29] used GCMC simulations to discuss the effect of kerogen maturity and moisture content on CH_4 adsorption capacity and adsorption heat on type II kerogens. However, it should be noted that since actual kerogens are complex and heterogeneous macromolecules, the present average structures used as models are difficult to capture all of the structure details. Although many efforts have be made to involve important kerogen structure details and improve the rationality of kerogen molecular structures, it is essential to validate these structures by comparing simulated adsorption isotherms with experimental data before analyzing gas adsorption mechanism. Moreover, in addition to kerogen component, mineral component of shale also contributes to the overall adsorption capacity. Unfortunately, representative shale molecular models involving both kerogen and mineral components remain to be developed and improved. So far, gas adsorption behaviors on kerogen and mineral components are mainly separated investigated for the molecular simulation studies in the literature. Although many efforts have been devoted to understanding the effect of maturity and moisture content on gas adsorption capacity, to our best knowledge, the microscopic adsorption mechanisms of pure CH_4, CO_2 and their binary mixtures on different mature kerogens with the presence of various moisture contents have not been investigated so far, and our work aims to gain insights into this topic.

In this work, we focused on the type II kerogen from the organic-rich shale formation [30]. Four different mature kerogen units from the work of Ungerer et al. [31] were selected to develop the bulk kerogen models through the MD method. Based on these realistic kerogen models, the adsorption behaviors of pure CH_4, CO_2 and their binary mixtures associated with various moisture contents (0, 0.7, 1.4, 2.1, 2.8 wt%) were investigated by GCMC simulations. The influences of kerogen maturity and moisture content on the adsorption capacity, isosteric heat of adsorption and adsorption selectivity of gas molecules were discussed. To quantify the effect on adsorption capacity, the pore structural parameters of kerogen models of different maturities and moisture contents were calculated. The radial distribution function (RDF) was computed to analyze the affinity between CH_4/CO_2 molecules with atoms in the kerogen model. In the case of moisture effect on the isosteric heat of adsorption, the distributions of H_2O molecules in different mature kerogen models were visualized. This study is hoped to gain insights into the influence mechanisms of maturity and moisture content on adsorption behaviors of CH_4, CO_2 and their mixtures on kerogen and to provide theoretic guide for the project of enhanced shale gas recovery by CO_2 sequestration.

2. Computational methodology

2.1. Kerogen structure units

The structure units of kerogen models (Fig. A.1) adopted in this work were built by Ungerer et al. [31] referring to the analytical experimental data from the work of IFP-EN and Exxon researchers [32]. The four kerogen units correspond to the organic-rich marine shales from the Duvernay series at an increasing maturity from immature to postmature. The type II kerogen is not only typical source of conventional oil and gas resources, such as these in the North Sea and western Canada [31]. The mature kerogen IIC is representative of organic matter in unconventional liquid hydrocarbons reservoirs, similar to that in the Bakken shale [33,34], while the postmature kerogen IID is associated with organic matter in unconventional gas formations such as the Barnett shale [35]. The detailed structural and compositional parameters of these kerogen units can be found in the work of Ungerer et al. [31], which match fairly well with the results of analytical experiments including the solid-state C^{13} NMR spectroscopy and X-ray techniques [32].

2.2. Molecular models of bulk kerogen

The condensed bulk kerogen models are generated through a combination of geometry optimization and MD simulations in Materials Studio using COMPASS force field [36]. This all-atom force field adopts the molecular potential of Lennard-Jones 6–9 to describe the dispersion-repulsion interactions between atomic pairs. It is widely used for its high accuracy in thermodynamic properties prediction for both organic and inorganic compounds in condensed phase [37].

Initially, the structures of kerogen units are relaxed by geometry optimization and annealing simulations [38]. We adopt the smart minimization algorithm with a fine convergence criterion to optimize the structure geometry. The non-bonded interactions including Coulomb and Van der Waals are calculated based on atom [38], and a fine cutoff distance of 15.5 Å is adopted. For the annealing method, 10 annealing cycles with increasing temperature from 300 to 800 K are selected. The simulations are carried out with the canonical ensemble (NVT) [37], in which the molecular number, box volume and system temperature are fixed, and a total simulation time of 400 ps is executed to bring the structures to the lowest energy state.

Thereafter, 6–12 optimized kerogen units are enclosed in a big simulation box with periodic boundary conditions to generate the initial configurations of kerogen models, with the target density being 0.1 g/cm^3 [29,31,34]. The number of kerogen units for each kerogen model is determined to guarantee similar system size and computational

workload. The subsequent relaxation process refers to the procedure adopted by Zhao et al. [29], Ungerer et al. [31] and Collell et al. [34]. These configurations are relaxed by a succession of MD simulations [29,31,34]. NVT ensemble is firstly adopted to relax the configurations at 800 K for 200 ps. Then succeeding NPT (fixed molecular number, system temperature and pressure) simulations are performed at 200 bar with a stepwise decreasing temperature from 800 to 300 K [34]. The simulation time of each run for the NPT simulation is 300 ps, which is sufficient for the density convergence of these kerogen models [31,34]. At last, these configurations are further simulated at 300 K and 1 bar for 400 ps to reach the equilibrium states of these kerogen models (Fig. A.2). To investigate the effect of moisture content on gas adsorption on kerogen models, moist kerogen models with a series of moisture contents (0.7, 1.4, 2.1 and 2.8 wt%) are constructed through the fixed loading task in Sorption module of Materials Studio, as adopted in the work of Liu et al. [28]. The range of moisture contents is consistent with the kerogen moisture contents of experimental investigations [39] and simulation work [27,29].

2.3. Simulation details

The adsorption behaviors of CH_4, CO_2 and their mixtures on dry and moist kerogen models are simulated by GCMC method using COMPASS force field [28,37]. The Van der Waals interactions are atom-based with a fine cutoff distance of 15.5 Å, while the Coulombic interactions are summed by the Ewald method, as adopted in the work of Liu et al. [28] and Sui et al. [37]. The temperature is imposed with the Andersen thermostat. For each pressure point of the isotherm, the first 5×10^6 Monte Carlo steps are performed to achieve the equilibrium state, while another 1×10^7 steps are taken as production stage to obtain the adsorption capacity [37].

During the GCMC simulations, the fugacity instead of pressure of gas molecules is applied to predict the adsorption capacity. The fugacity is converted from pressure with the fugacity coefficient, which can be calculated by the Peng-Robinson equation [40]. The simulation produces the absolute adsorption capacity of gas molecules. All the absolute adsorption isotherms in this work are fitted with the Langmuir model,

$$n^{\alpha} = n^{\alpha}_{\max}\frac{bp}{1+bp} \tag{1}$$

where n^{α} is the gas absolute adsorption capacity, $n^{\alpha}_{\max}$ is the Langmuir maximum adsorption capacity (LMAC), p is the pressure, and b is the Langmuir constant. To compare the simulated adsorption isotherms with experimental results, the excess adsorption capacity is computed by [29],

$$n^{e} = n^{\alpha} - \upsilon\rho \tag{2}$$

where n^{e} is the excess adsorption capacity, ρ is the gas density calculated by the Peng-Robinson equation, and υ is the free pore volume of kerogen determined using the Atom Volumes & Surface tool in Materials Studio. The pore volumes are detected by a probe molecule of given radius. The probe molecule rolls over the van der Waals surface of the skeleton atoms to determine the surface of solid skeleton. The regions left by the surface of solid skeleton are identified as pore volumes.

The isosteric heat of adsorption is an important thermodynamic parameter for evaluating the interaction strength between gas molecules and kerogen skeleton, which can be determined by the Clausius-Clapeyron equation [41],

$$Q_{st} = RT^2\left(\frac{\partial \ln p}{\partial T}\right)_n \tag{3}$$

where Q_{st} is the isosteric heat of adsorption at the absolute adsorption amount of n, kJ/mol, R is the universal gas constant, kJ/(mol·K), T is the temperature, K, p is the pressure, kPa.

To investigate the influence of maturity and moisture content on the competitive adsorption behaviors of CO_2 and CH_4, the adsorption selectivity of the binary mixtures is calculated, which is defined as [28],

$$S_{CO_2/CH_4} = \frac{x_{CO_2}/x_{CH_4}}{y_{CO_2}/y_{CH_4}} \tag{4}$$

where S_{CO_2/CH_4} is the adsorption selectivity of CO_2 over CH_4, x_i is the mole fraction of component i in the adsorption phase, while y_i is the mole fraction of component i in the bulk phase. The adsorption selectivity represents the relative adsorption strength of CO_2 and CH_4 on the kerogen models. A higher selectivity indicates a stronger adsorption capacity of CO_2 compared to that of CH_4.

The pore size distribution is computed using the method of probe insertion. Spherical probes of stepwise increasing radius (0.5–3 Å) are randomly inserted into the system, and the regions where the probe molecules do not overlap with the skeleton atoms are accepted as free pore volumes. Thus, the pore size distribution is obtained by differentiating the free pore volumes under different sizes of probe molecules.

Moreover, the contribution of different kinds of pores to total pore volumes is also computed using the probe insertion method. A probe with a zero radius is firstly adopted to detect the total pore volumes in the kerogen models. Thereafter, a probe with a radius of 2 Å is inserted into the kerogen models to compute the volumes of enterable pores (diameter ≥ 4 Å). The volumes of ineffective pores (diameter < 4 Å) are obtained by reducing the volumes of enterable pores from the total pore volumes.

3. Results and discussion

3.1. Force field and molecular model validation

In this section, we firstly validate the force field by comparing the geometry parameters and condensed-phase densities of CH_4, CO_2 and H_2O molecules with experimental results, then we examine the consistency of kerogen densities and excess adsorption isotherms between simulated and experimental results to validate the kerogen models.

The geometry parameters of small molecules optimized by different force fields are shown in Table A.1. Remarkably, the bond lengths and bond angles optimized by COMPASS force field are closer to the experimental data [42] compared with those given by pcff and Dreiding force fields. To further validate COMPASS force field, the experimental and simulated condensed-phase densities of CH_4, CO_2 and H_2O molecules at 353 K are illustrated in Fig. A.3. The simulated densities for CH_4 and CO_2 using COMPASS force field are in good agreement with the experimental data [42], while the predicted densities of H_2O molecules are slightly smaller than the documented data [42] at low pressure. Overall, the simulated properties of isolated small molecules and their condensed phase by COMPASS force field are reasonably consistent with the experimental data [42], thus COMPASS is selected as the appealing force field in this work.

Physical density is an important criterion for evaluating the reasonability of molecular model. Our simulated densities of kerogen models are compared with documented experimental data at ambient conditions. The density of our immature kerogen model (IIA) is 1.07 g/cm^3, consistent with the experimental density (1.0–1.15 g/cm^3) of immature type II kerogen in New Albany Shale [43]. The densities of our IIB and IIC models in the oil window are 1.16 and 1.18 g/cm^3, respectively, which are close to the pyrite-free type II kerogen densities (1.18–1.25 g/cm^3) at the similar maturity [44]. The simulated density of the postmature kerogen IID model (wt%, carbon 85.16, hydrogen 4.1, nitrogen 2.27, oxygen 5.84) is 1.185 g/cm^3, which is fairly close to

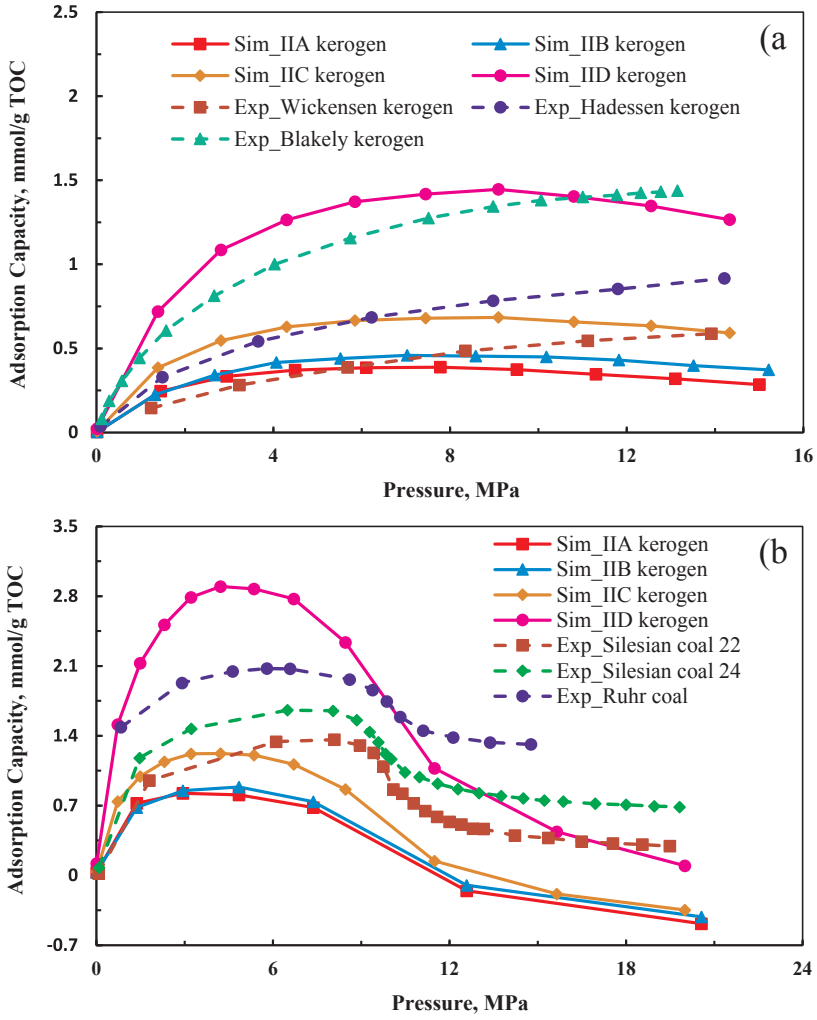

Fig. 1. Comparison of excess adsorption isotherms of CH_4 and CO_2 between simulated and experimental results: (a) CH_4 excess adsorption isotherms at 338 K; (b) CO_2 excess adsorption isotherm at 318 K.

the experimental value (1.181 g/cm^3) of an ash-free bituminous coal with the similar compositions (wt%, carbon 86.50, hydrogen 5.0, nitrogen 2.0, oxygen 5.95) [45] The densities of our kerogen models increase with maturity, which is consistent with the conclusion of previous simulation work [29,31] and experimental investigations [44].

The excess adsorption isotherms of CH_4 and CO_2 on kerogen models of different maturities are simulated, and compared with the measured results in laboratory (Fig. 1). The experimental data for CH_4 excess adsorption are carried out on the kerogen samples of Posidonia shale in Wickensen well (R_o = 0.53%) and Hadessen well (R_o = 1.45%) [46] and the kerogen sample of Barnett shale in Blakely well (R_o = 2.01%) [47]. The experimental data are normalized by the TOC to compare with our simulated results. The experimental CO_2 excess adsorption isotherms are performed on coal samples of different maturities, including Silesian coal sample 22 (R_o = 1.2%) [48], Silesian coal sample 24 (R_o = 1.8%) [48] and Ruhr coal sample (R_o = 3.3%) [24]. The experimental results for CO_2 excess adsorption are also normalized by the TOC. For the CH_4 excess adsorption isotherms, our simulated results present the same trend with experimental data that the CH_4 excess adsorption capacity increases with kerogen maturity. The maximal CH_4 excess adsorption capacity for IID model is 1.45 mmol/g, fairly close to the normalized experimental result of Blakely kerogen (1.44 mmol/g). For the CO_2 excess adsorption isotherms, the consistent trend between the simulated and experimental isotherms is observed, namely, the CO_2 excess adsorption capacity initially increases, and then deceases as the pressure increases, which has also been reported by Wu et al. [49]. Moreover, the simulated CO_2 excess adsorption capacity also increases with the maturity, which is consistent with the experimental results.

Differences in the excess adsorption isotherms in Fig. 1 can be attributed to the discrepancies of thermal maturity, molecular structure and inorganic content between our kerogen models and the experimental samples. Lu et al. [50] have reported that thermal maturity plays a key role in gas adsorption capacity by laboratory study. Because our kerogen models are not derived from the experimental samples used for comparison in Fig. 1, the thermal maturities of our kerogen models are not exactly coincident with the experimental samples in Fig. 1. Similarly, the molecular structures between the experimental samples and our kerogen models are not completely consistent, which can influence the excess adsorption isotherms. Moreover, the existence of inorganic matter in the experimental samples can also contribute to the differences in the excess adsorption isotherms. It should be noted that although our simulated excess adsorption isotherms cannot be perfectly fitted by the documented experimental data, the magnitude of excess adsorption capacity and the tendency for excess adsorption capacity changing with pressure and thermal maturity conform to the documented experimental results. Zhao et al. [29] validated their kerogen models by comparing simulated CH_4 excess adsorption isotherms with documented experimental data. Similar with our study, they obtained the same magnitude of CH_4 excess adsorption capacity and the same trend of CH_4 excess adsorption isotherms with respect to

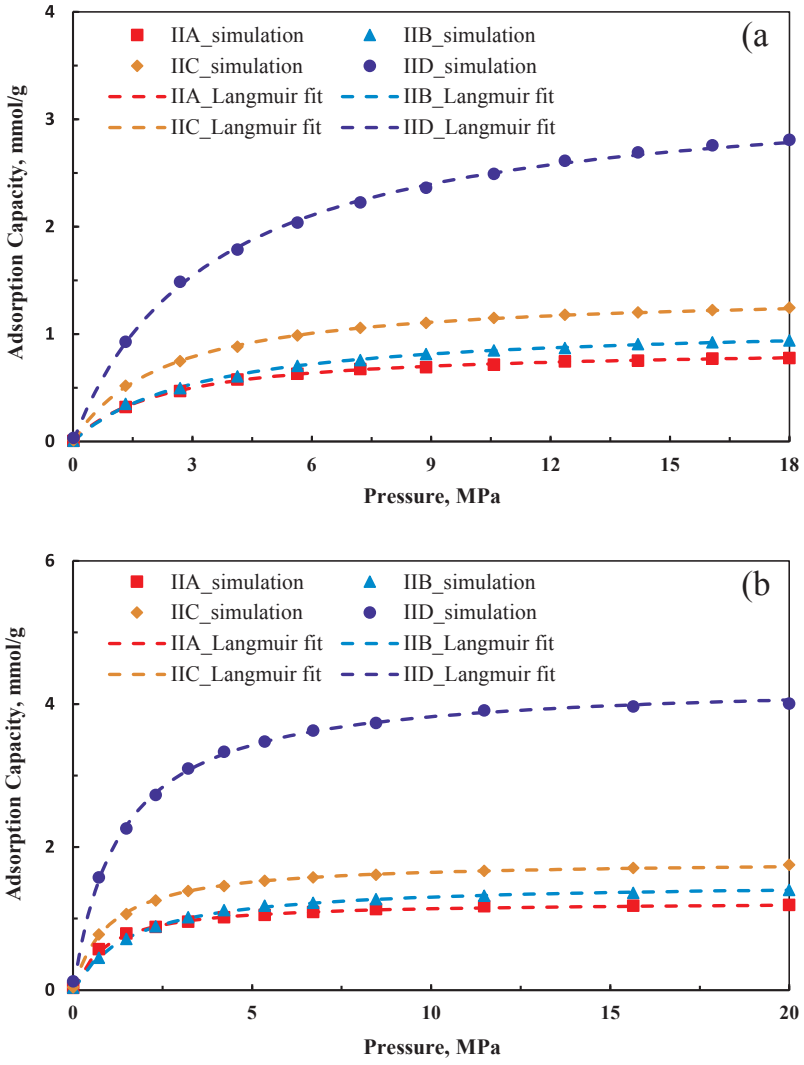

Fig. 2. Absolute adsorption isotherms of pure gases on different mature kerogen models at 318 K: (a) CH_4 absolute adsorption isotherms; (b) CO_2 absolute adsorption isotherms.

pressure and thermal maturity, which were used as good indications for the reasonability of their kerogen models. Accordingly, our kerogen models in this work are reasonable, and can be utilized to investigate the adsorption behaviors of CH_4 and CO_2.

3.2. Pure gases adsorption on dry bulk kerogen models

Initially, the pure CH_4 and CO_2 adsorptions on dry kerogen models are simulated using the GCMC method to study the effect of maturity on adsorption capacity. Absolute adsorption isotherms of pure gases on different mature kerogen models at 318 K are plotted in Fig. 2. The isotherms are fitted by the Langmuir model, and the fitting parameters are listed in Table A.2. The Langmuir model is observed to have good fitting accuracy for both CH_4 and CO_2 absolute adsorption isotherms on different mature kerogen models. The absolute adsorption capacity of CH_4 and CO_2 increases with increasing pressure, and tends to reach adsorption equilibrium at high pressure. Remarkably, the absolute adsorption capacity of CO_2 is much higher than that of CH_4. Besides, the CO_2 absolute adsorption isotherms reach the adsorption equilibrium at lower pressure, indicating a higher adsorption rate of CO_2 over CH_4. Moreover, as seen in Table A.2, the LMAC of CH_4 and CO_2 increases as the kerogen maturity increases, which is consistent with previous experimental study for CH_4 adsorption on Posidonia shales of different maturities [46].

To further investigate the effect of pore structure characteristics on gases adsorption capacity, porosities and specific surface areas of kerogen models are calculated through the Atom Volumes & Surface tool in Materials Studio, and the results are listed in Table A.3. The porosities of our kerogen models (15.1–27.6%) are close to the documented porosities (20–25%) of kerogen samples with SEM images [51], which further validates the reliability of our kerogen models. As seen in Table A.3, the porosity of the kerogen models increases with increasing maturity, while the specific surface area shows an initial increase and then a decreases as the maturity increases. This evolution of porosity and specific surface area with maturity has also been reported by Chen et al. [52] based on porous structure investigations on a suite of different mature shale samples. Chen et al. divided the evolution of nanopores in organic matter into two main stages (regardless of the influence of bitumen), namely the developing stage and the conversion and destruction stage. This evolution trend can be illustrated by the pore structure of kerogen (Fig. 3). Fig. 3a and b reflects the developing stage of nanopores. In this stage, a large number of tiny pores are generated, and most of these tiny pores are isolated and ineffective, leading to the increase of porosity and specific surface area. Fig. 3b–d belongs to the conversion and destruction stage. In this stage, the enlargement of pore size contributes to the increasing porosity and decreasing specific surface area. For Fig. 3c, some of these tiny pores collapse and merge into small pores, but the connectivity between these

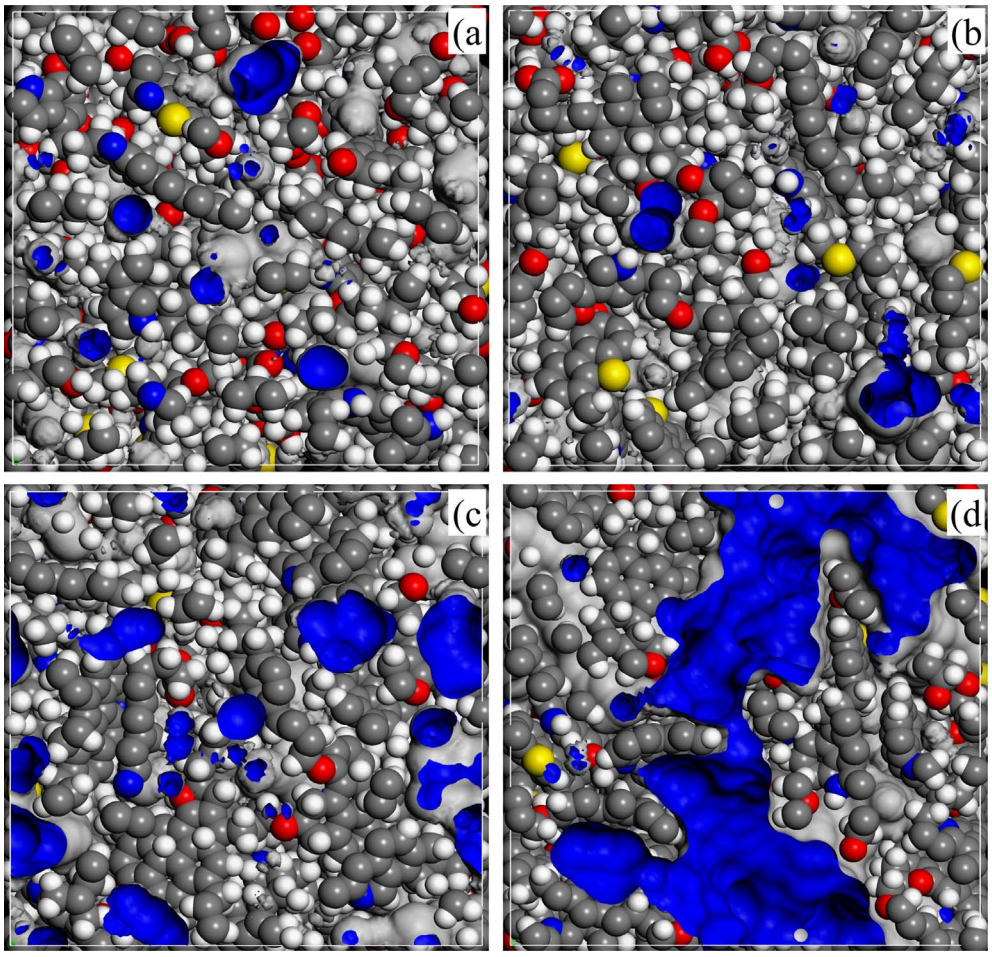

Fig. 3. Pore structures of different mature kerogen models at 318 K: (a) IIA kerogen model, cell length is 31.3 Å; (b) IIB kerogen model, cell length is 31.6 Å; (c) IIC kerogen model, cell length is 31.0 Å; (d) IID kerogen model, cell length is 31.7 Å. Atom representation: grey for carbon atoms, white for hydrogen atoms, red for oxygen atoms, yellow for sulfur atoms. The pore volumes are indicated by the blue regions. (For interpretation of the references to colour in this figure legend, the reader is referred to the web version of this article.)

small pores is still poor. For Fig. 3d, these small pores develop into effective pores, and these effective pores are highly connected. Pore size distributions and contributions of different kinds of pores to total pore volumes are presented in Fig. 4. It should be noted that we only compute the pore size distributions over a small range of pore sizes due to the relatively small system size of kerogen models. For IIA and IIB, the computed pore size distributions cover most of the pores in the system because ineffective pores (diameter < 4 Å) are dominated pore types (Fig. 4b), while for IIC and IID, a large number of pores with bigger sizes are not presented in the pore size distributions since volumes of enterable pores (diameter ≥ 4 Å) take a large share of the total pore volumes in the two kerogen models (Fig. 4b). Accordingly, the effective pore volumes of kerogen models increase during the thermal maturation, which may account for the increasing adsorption capacity with maturity.

To investigate the thermodynamic property of gas adsorption on kerogen, the isosteric heat of adsorption for the four kerogen models under different coverages is plotted in Fig. A.4. The isosteric heat decreases as the adsorption coverage increases for IIA, IIB and IIC kerogen models, which can be attributed to the energetic heterogeneity of kerogen surface [53–55]. Gas molecules are preferentially adsorbed on the high-energy adsorption sites at the beginning of adsorption, and then tend to occupy the adsorption sites of weaker energy as the adsorption proceeds. Interestingly, the isosteric heat of adsorption decreases at the beginning, and then increases with increasing adsorption coverage for IID kerogen model. The later increase of isosteric heat has also been observed by Sui et al. [37], who attributed it to the non-negligible contribution of adsorbate-adsorbate interaction to the adsorption enthalpy at high coverage. The isosteric heat at zero coverage is defined as the limit isosteric heat, which reflects quantitatively the adsorption enthalpy between adsorbent and adsorbate without the influence from the adsorbate-adsorbate interaction. We average the limit isosteric heat on four different configurations for each kerogen model to reduce the uncertainty brought by initial configurations. The limit isosteric heat for CH_4 adsorption is IID (24.1 ± 0.2 kJ/mol) > IIC (22.1 ± 0.2 kJ/mol) > IIB (21.5 ± 0.3 kJ/mol) > IIA (21.4 ± 0.3 kJ/mol), while that for CO_2 adsorption is IID (32.1 ± 0.3 kJ/mol) > IIC (30.5 ± 0.3 kJ/mol) > IIA (30.1 ± 0.3 kJ/mol) > IIB (29.6 ± 0.3 kJ/mol). The order of limit isosteric heat is consistent with the initial slopes of the absolute adsorption isotherms for gas molecules on the four kerogen models, as indicated by Fig. 2.

It should be noted that the adsorption enthalpy actually results from the combination of the adsorbate-adsorbent interaction and the adsorbate-adsorbate interaction, as concluded by Sui et al. [37]. To consider the contribution of both the two kinds of interactions, we calculate the average isosteric heat of adsorption, defined as the arithmetic average of the isosteric heat of gas adsorption under different surface coverages, to reflect the realistic thermodynamic property based on Fig. A.4. For CH_4 adsorption, the sequence of average isosteric heat of adsorption for different mature kerogen models is IIB (20.7 kJ/mol) > IIC (20.6 kJ/mol) > IIA (20.4 kJ/mol) > IID (18.5 kJ/mol), while for CO_2 adsorption, the average isosteric heat of adsorption is in the following order: IIA (28.7 kJ/mol) > IIB (27.7 kJ/mol) > IID (26.6 kJ/mol) > IIC (26.1 kJ/mol). These values of CH_4 are in the range of previous experimental data for coal (10–22 kJ/mol) [56] and activated carbon (16–20 kJ/mol) [57], while the results of CO_2 match fairly with the documented data for activated carbon (29.12 kJ/mol) [58]. The

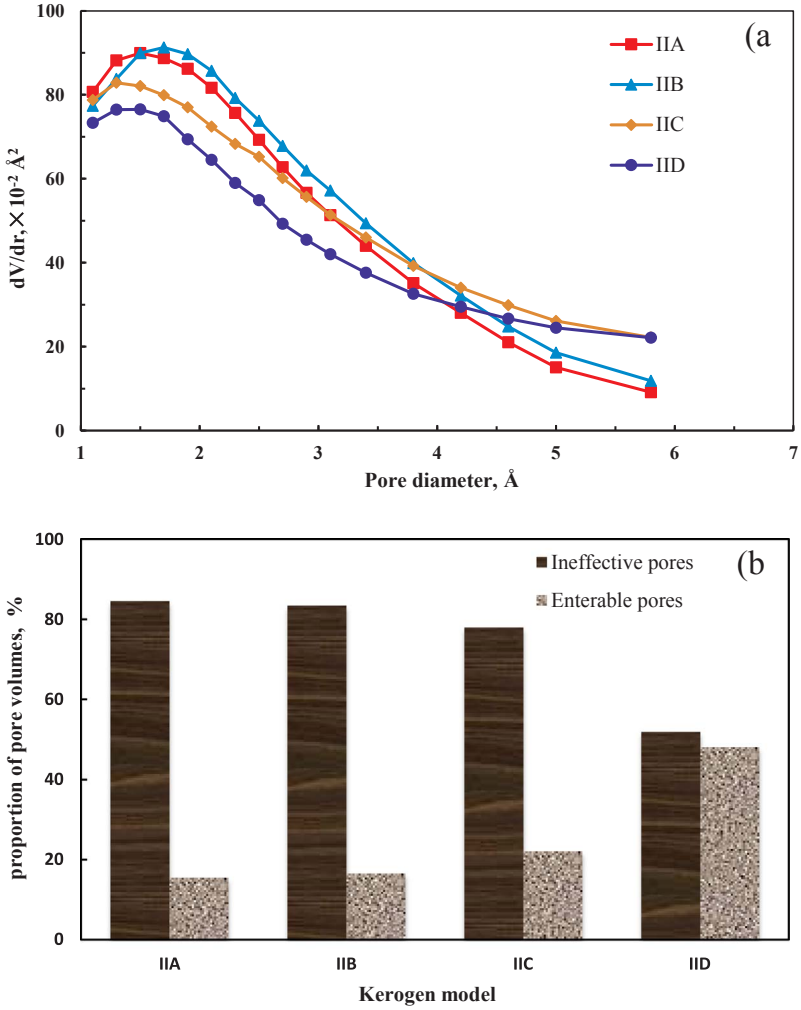

Fig. 4. Pore structure properties of different mature kerogen models: (a) pore size distribution; (b) contribution of different kinds of pores to total pore volumes.

average isosteric heat of CO_2 adsorption (26.1–28.7 kJ/mol) is larger than that of CH_4 adsorption (18.5–20.7 kJ/mol), which indicates that CO_2 is preferentially adsorbed on kerogen models compared with CH_4. Remarkably, the isosteric heat of adsorption does not present a consistent trend with kerogen maturity, identical with previous experimental results on Barnett shale [21]. The order of isosteric heat of CH_4 adsorption is found to be consistent with the sequence of specific surface area of different kerogen models listed in Table A.3.

Fig. 5 presents the RDFs between gas molecules and different atoms of kerogen. Due to the similarity of kerogen composition, we only present the results for kerogen IIA. The RDF describes the loading probability of a certain particle as a function of distance from a reference particle, which can reflect the affinity between the two particles. Apparently, the RDF between CH_4 and sulfur atom in the first peak is sharper than the values of other pairs (Fig. 5a), indicating that CH_4 is preferentially adsorbed on the sites of sulfur atoms of kerogen. As seen from Fig. 5b, the first peaks of RDFs between CO_2 and sulfur/oxygen atoms are higher than other first peaks, which suggests that CO_2 preferentially occupies the sites of sulfur and oxygen atoms of kerogen. We can infer that the sites associated with sulfur atom are the primary sites in kerogen for competitive adsorption between CH_4 and CO_2. Zhang et al. [27] attributed the high gas adsorption heat to the presence of sulfur in the coal structure. Similarly, in our work, the sequence of sulfur/oxygen content with respect to carbon atoms ((S + O)/C) of the kerogen models is IIA (10.7%) > IIB (6.8%) > IID (6.3%) > IIC (6.2%), which is consistent with the order of average isosteric heat of CO_2 adsorption.

3.3. Mixed gases adsorption on dry bulk kerogen models

To reveal the effect of maturity on competitive adsorption of CH_4 and CO_2, the adsorption behaviors of mixed gases with various mole ratios on our kerogen models are simulated through the GCMC method. The LMACs of gas molecules of different CO_2 mole fractions on the four kerogen models are presented in Fig. 6. Manifestly, the LMACs of CH_4 decrease, while these of CO_2 increase with increasing CO_2 mole fraction. The LMACs of CO_2 are larger than those of CH_4 once after the CO_2 mole fractions exceed 0.24, 0.32, 0.34 and 0.35 for kerogen IIA, IIB, IIC and IID, respectively. Moreover, the LMACs of both CH_4 and CO_2 in the mixed gases increase with increasing kerogen maturity, which is accordant with the conclusion for pure gases adsorption in Section 3.1.

Fig. 7 illustrates the CO_2/CH_4 adsorption selectivity on our kerogen models as a function of pressure and CO_2 mole fraction. The selectivity varies between 1.5 and 5.7 in the investigated range of pressures and CO_2 fractions, indicating that CO_2 is energetically more favorable than CH_4 to be adsorbed on the kerogen models. The range of the selectivity is close to the reported simulated results (2.3–8.9) on coal [59]. For our different mature kerogen models, the same trend has been observed that the selectivity decreases gradually with the rise of bulk pressure, and then reaches the equilibrium value at high pressure. This trend can be attributed to the energetically heterogeneous characteristic of kerogen surface. At the initial stage of competitive adsorption, the high-energy sites are preferentially occupied by CO_2, causing a higher selectivity. As the pressure increases, CH_4 and CO_2 molecules begin to

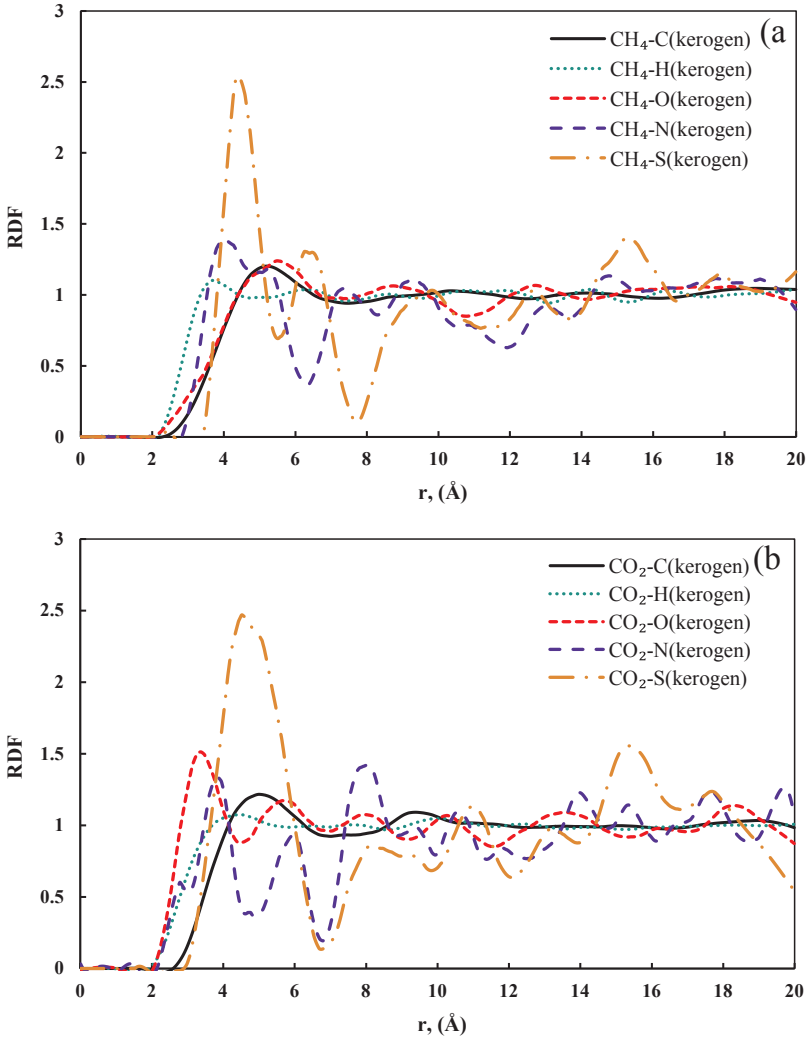

Fig. 5. Radial distribution functions between gas molecules and atoms of kerogen IIA at 318 K: (a) CH_4; (b) CO_2.

competitively occupy the energetically weaker sites, decreasing the selectivity till the equilibrium state. As seen from Fig. 7a and b, the selectivity decreases with increasing CO_2 mole fraction for the lower mature kerogen models (IIA and IIB), which is consistent with previous investigation results [59,60]. The same phenomenon can be observed for the higher mature kerogen models (IIC and IID) (Fig. 7c and d) when the pressure exceeds 9 and 15 MPa, respectively. However, an opposite trend is found at low pressure for IIC and IID models that the selectivity increases with the CO_2 mole fractions. This may be explained by the pore structure differences between the kerogen models, as analyzed in

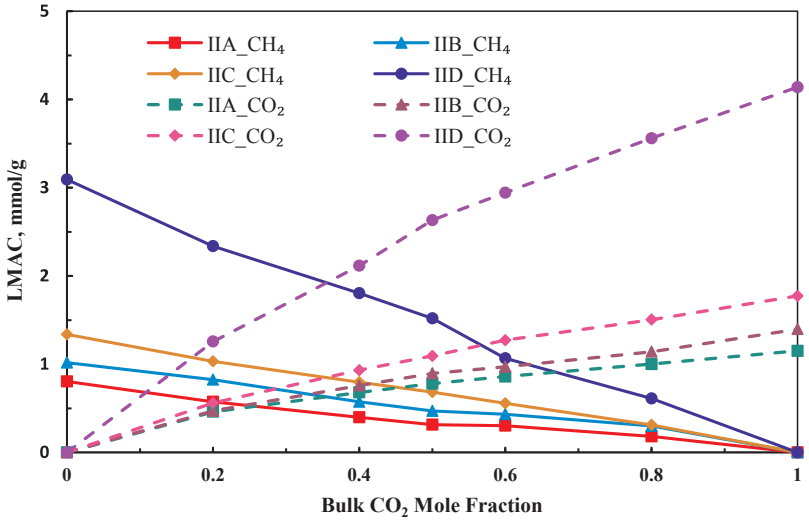

Fig. 6. LMAC of gas molecules for different CO_2 mole fractions on different mature kerogen models.

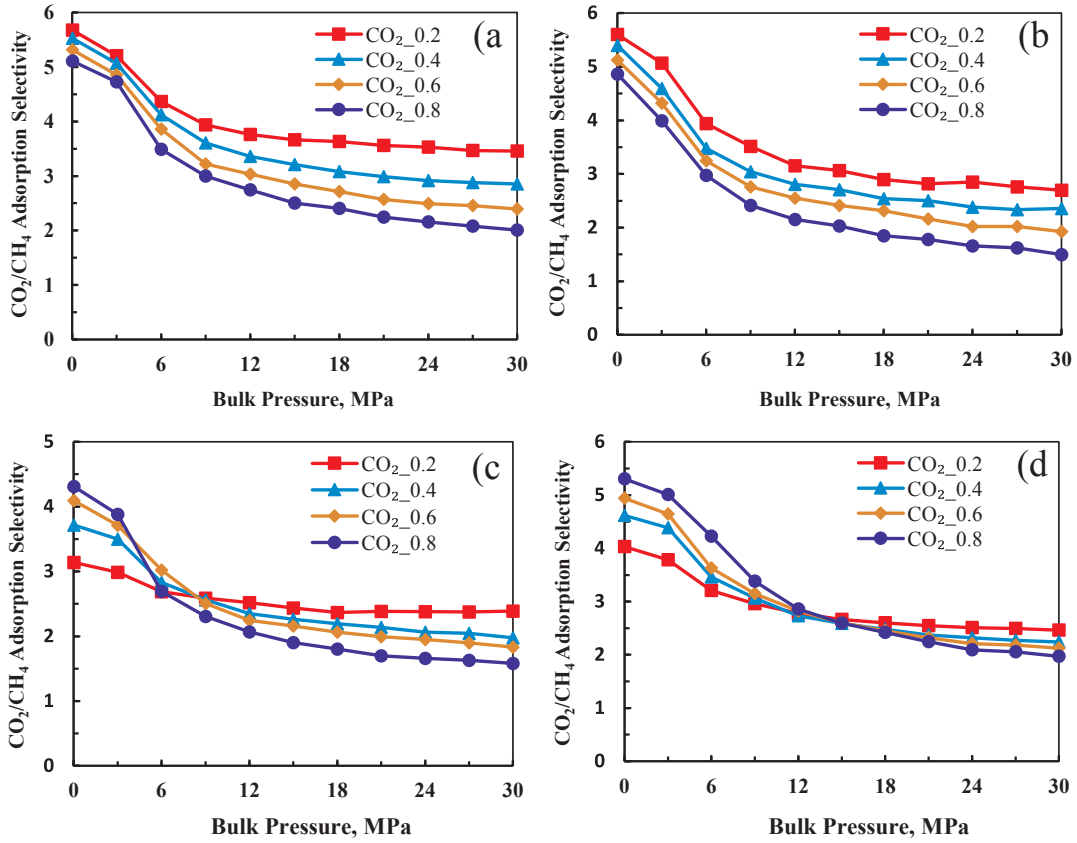

Fig. 7. CO_2/CH_4 adsorption selectivity for different CO_2 mole fractions and pressures on different kerogen models: (a) IIA kerogen model; (b) IIB kerogen model; (c) IIC kerogen model; (d) IID kerogen model.

Section 3.2. Small pores are dominated pore types for kerogen IIA and IIB, while effective big pores take a large share of the total volumes of kerogen IIC and IID. For small pores, as well as big pores at high pressure, CO_2 molecules have to compete with both CH_4 molecules and CO_2 molecules for limited adsorption sites. The increasing CO_2 mole fraction leads to the increase of CO_2–CO_2 interaction, thus hindering the CO_2-adsorbent interaction. While for big pores at low pressure, since the adsorption sites are sufficient to accommodate the CO_2 molecules, the CO_2–CO_2 interaction is not significant compared with the CO_2-adsorbent interaction. Thus the increase of CO_2 mole fraction facilitates the preferential adsorption of CO_2.

3.4. Effect of moisture on pure gases adsorption

In this section, the influence of pre-adsorbed H_2O molecules on pure gases adsorption on our kerogen models is investigated through the GCMC simulations. Fig. 8 shows the LMACs and porosities of kerogen models, which are averaged by three different configurations for each kerogen structure to reduce the uncertainty brought by initial configurations. The effective porosity is probed by CH_4 and CO_2 molecules for Fig. 8a and b, respectively. As the moisture content increases, the effective porosity presents a linear decrease, indicating that the pre-adsorbed H_2O molecules occupy the effective pore volumes for gas molecules adsorption. As a result, the LMAC of CH_4 and CO_2 also decreases linearly with increasing moisture content. Table A.4 lists the LMAC reduction of CH_4 and CO_2 for different moisture contents. Remarkably, the LMAC reduction of gas molecules decreases with the increase of kerogen maturity at higher moisture contents, indicating that the negative influence of moisture on the LMAC decreases with increasing kerogen maturity. This trend can be attributed to the decomposition of hydrophilic groups and the enlargement of pore sizes during the kerogen maturation evolution. H_2O molecules are preferentially adsorbed on the hydrophilic groups on the kerogen surface, aggregating into clusters at higher moisture contents [14]. These clusters are widely distributed in the lower mature kerogen models, which can easily block the small pores accessible for gas molecules. In contrast, the effect of moisture on the LMAC becomes less significant for the higher mature kerogen models, since the hydrophilic groups are more limited and the pore sizes are bigger.

To study the effect of moisture on the thermodynamic property of gases adsorption, the average isosteric heat of adsorption with different moisture contents is calculated, and the results are plotted in Fig. 9. The presented isosteric heat is also averaged by three different configurations for each kerogen model. For kerogen IIA and IIB models, as the moisture content increases, the isosteric heat of CH_4 adsorption fluctuates weakly, while that of CO_2 adsorption decreases at the beginning and then becomes smooth with the further increase of moisture content. Most of the pre-adsorbed H_2O molecules are located in the middle of pores due to the hydrophobic characteristic of kerogen carbon skeleton, while a small portion of H_2O molecules are adsorbed on the hydrophilic groups. (Figs. A.5 and A.6). As discussed in Section 3.2, the isosteric heat of CH_4 adsorption is correlated with the specific surface area, while that of CO_2 adsorption is associated with the functional groups. Because H_2O molecules in the middle of pores have a small effect on the surface area, the isosteric heat of CH_4 adsorption changes a little with moisture content. Meanwhile, since the accessible hydrophilic adsorption sites are limited, the CO_2 isosteric adsorption heat only decreases significantly at lower moisture contents when these accessible sites are not fully filled. For kerogen IIC model, the isosteric heat of CH_4 and CO_2 adsorption changes moderately at lower moisture contents and then

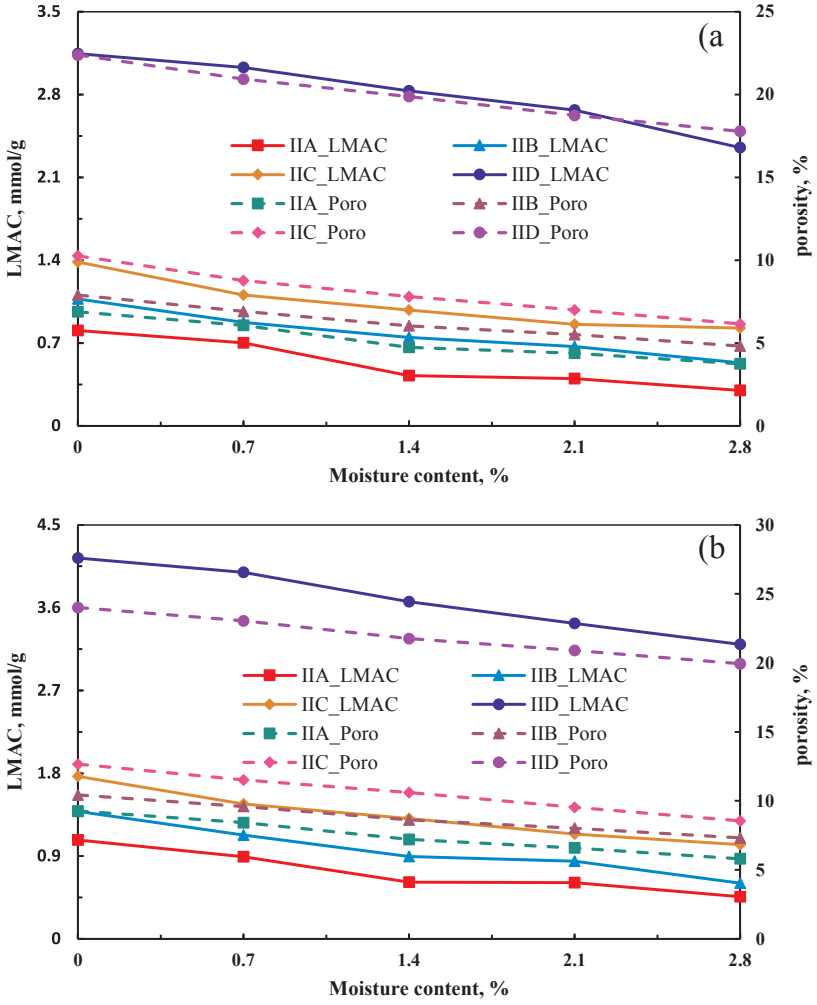

Fig. 8. Average LMACs and effective porosities with different moisture contents: (a) CH_4; (b) CO_2.

increase when the moisture content is higher. As seen in Fig. A.7, H_2O molecules aggregate into small clusters and distribute in the middle of pores at lower moisture contents (Fig. A.7a–c), causing a small effect on the surface area and adsorption sites. The later increase of the isosteric adsorption heat can be attributed to the migration of H_2O molecules and the squeeze effect of growing H_2O molecules clusters. As shown in Fig. A.7c and d, some H_2O molecules, which originally occupy some high-energy adsorption sites, are observed to migrate and aggregate into clusters with a larger size. It should be noted that the migration and aggregation of H_2O molecules can release some occupied high-energy adsorption sites to be potentially adsorbed by gas molecules, thus increasing the gas isosteric adsorption heat. In addition, as shown in Fig. A.8, there are still some high-energy adsorption sites in the kerogen model that are not occupied by H_2O and CH_4/CO_2 molecules even at saturated pressure conditions due to the physically and chemically heterogeneous structure of the kerogen model. With the increase of moisture content from 2.1 to 2.8 wt%, some CH_4/CO_2 molecules are observed to be squeezed to the adjacent high-energy adsorption sites by the growing clusters (Fig. A.8a–b and c–d), which contributes to the increasing gas isosteric heat. As for kerogen IID model, the isosteric heat of gases adsorption decreases at the beginning and then increases with further increasing moisture content. The postmature IID model is highly ordered, with the kerogen units presenting a parallel slice structure (Fig. A.9). Therefore, H_2O molecules can easily diffuse to the high-energy sites at lower moisture content (Fig. A.9a), decreasing the isosteric heat of adsorption. Moreover, similar with that of kerogen IIC model, some H_2O molecules are observed to migrate and aggregate into growing clusters at higher moisture content (Fig. A.9c and d), which contributes to the increasing isosteric adsorption heat.

3.5. Effect of moisture on mixed gases adsorption

In this section, the effect of moisture on mixed gases adsorption on our kerogen models is investigated by GCMC simulations. Fig. 10 shows the LMAC of mixed gases on kerogen models with various moisture contents. The LMAC of both CH_4 and CO_2 decreases with increasing moisture content. As discussed in Section 3.4, H_2O molecules are preferentially adsorbed on the hydrophilic groups, converting the adsorbate-adsorbent interaction to the adsorbate-liquid interaction through the steric effect. Also, the pre-adsorbed H_2O molecules decrease the effective pore volumes accessible for gas molecules. The CO_2 LMAC decreases linearly with increasing moisture content, which is due to the synergistic effect of H_2O molecules on high-energy sites and effective pore volumes. The CH_4 LMAC decreases smoothly at the beginning and then decreases quickly when the moisture content is higher for IIA and IIB models. In contrast, for IIC and IID models, The CH_4 LMAC decreases fast at low moisture contents and then decreases smoothly with further increasing moisture content. The lower mature kerogen models (IIA and IIB) contain a large number of tiny pores inaccessible for gas molecules, and most of the functional groups remain

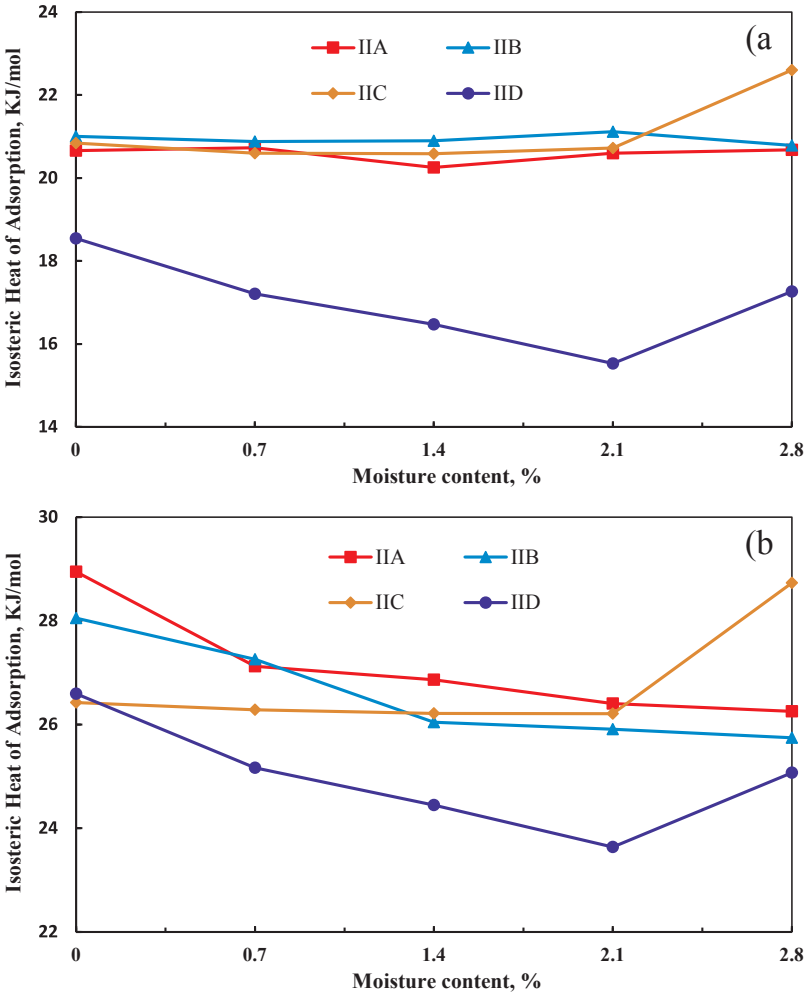

Fig. 9. Average isosteric heat of gases adsorption with different moisture contents: (a) CH_4; (b) CO_2.

on the kerogen surface. At low moisture contents, H_2O molecules either enter these tiny pores or adsorb on the kerogen surface (Figs. A.5a and A.6a), causing a small effect on the effective pore volumes. When the moisture content is high, H_2O molecules begin to form clusters around the hydrophilic sites (Figs. A.5c–d and A.6c–d), significantly decreasing the effective pores volumes. In contrast, the higher mature kerogen models (IIC and IID) consist of substantial effective pores, and most of the functional groups are decomposed. Thus H_2O molecules can aggregate into clusters at lower moisture contents (Figs. A.7a and A.9b), which can account for the early decrease of the CH_4 LMAC.

The CO_2/CH_4 adsorption selectivity on different mature kerogen models with various moisture contents is illustrated in Fig. 11. For higher mature kerogen models (IIC and IID), the selectivity gradually increases to the equilibrium value with increasing moisture content. This indicates that the adsorption capacity of CH_4 decreases faster than that of CO_2 with increasing moisture content. For kerogen IIA model, the selectivity changes moderately in the beginning and then increases quickly when the moisture content is higher. This is because that the pre-adsorbed H_2O molecules preferentially fill the tiny pores inaccessible for CH_4 and CO_2 (Fig. A.5a), and then aggregate into clusters in effective pores (Fig. A.5b and d), which decreases the CH_4 adsorption capacity more rapidly. For kerogen IIB model, the selectivity also changes smoothly at low moisture contents, but then decreases with the further increase of moisture content. This is because that kerogen IIB has a wider pore size distribution than IIA. The pre-adsorbed H_2O molecules (diameter 2.65 Å) enter not only the tiny pores but also a large number of small pores, which are accessible for CO_2 molecules (diameter 3.3 Å) but inaccessible for CH_4 molecules (diameter 3.8 Å). Therefore, the moisture reduces the adsorption capacity of CO_2 faster than that of CH_4 for kerogen IIB model at higher moisture contents.

4. Conclusions

In this work, we constructed four realistic kerogen models with different maturities by the MD method. The adsorption behaviors of CH_4, CO_2 and their mixtures on the kerogen models with various moisture contents were investigated using GCMC simulations. The effects of maturity and moisture on kerogen adsorption capacity and gas adsorption behaviors were discussed in detail.

Our results indicate that the adsorption capacities of CH_4 and CO_2 on kerogen are proportional to the effective pore volumes, which increase with maturity but decrease with moisture content. The negative effect of moisture decreases with increasing kerogen maturity at high moisture contents. When the moisture content is 2.8 wt%, the reduction of Langmuir maximum adsorption capacity for CH_4 and CO_2 on immature IIA kerogen model are 62.4% and 57.8%, respectively, while that on postmature IID model are 24.0% and 22.7%, respectively.

The isosteric heat of gas adsorption on kerogen is closely associated with the kerogen chemical compositions (especially for sulfur and oxygen) and the distribution and aggregation of H_2O molecules. The average heat of CO_2 adsorption on kerogen IIA (10.7% (S + O)/C) is 28.7 kJ/mol,

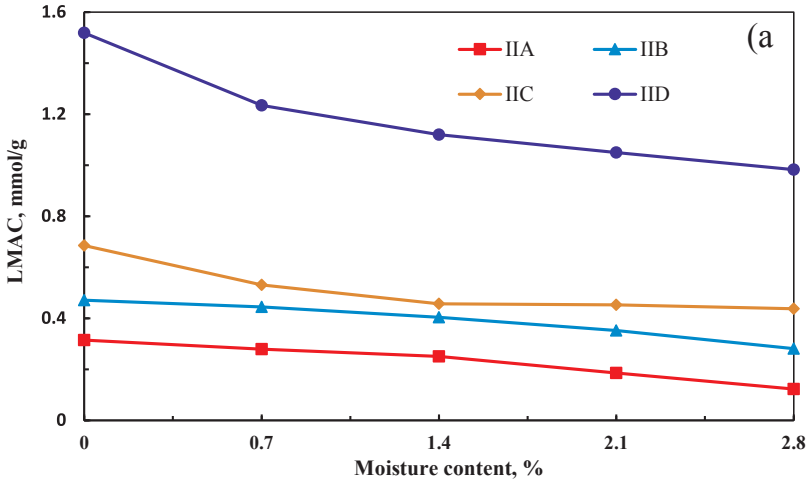

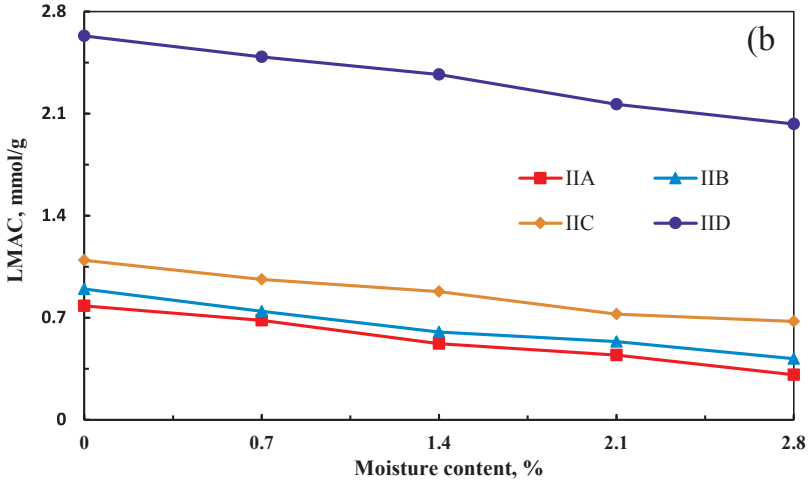

Fig. 10. LMAC of gas molecules with different moisture contents: (a) CH_4; (b) CO_2.

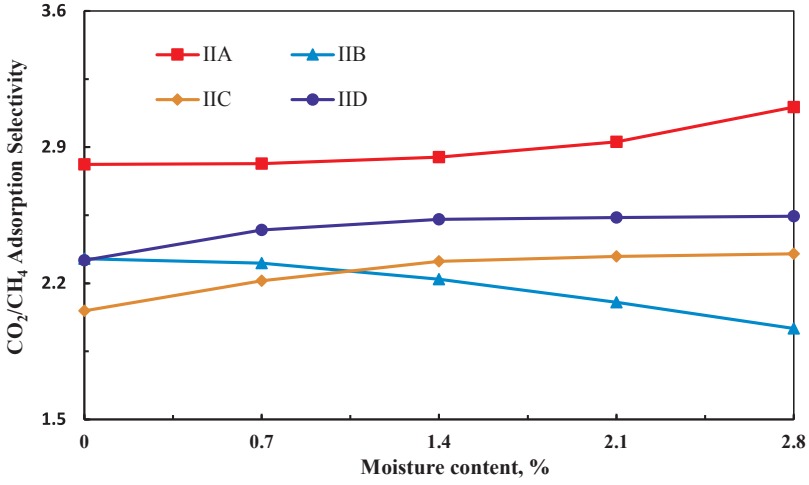

Fig. 11. CO_2/CH_4 adsorption selectivity on the kerogen models with different moisture contents.

while that on kerogen IIB (6.8% (S + O)/C), kerogen IIC (6.2% (S + O)/C) and kerogen IID (6.3% (S + O)/C) is 27.7, 26.1 and 26.6 kJ/mol, respectively. H_2O molecules located in the middle of kerogen pores exert a small effect on the adsorption heat of gas adsorption, while H_2O molecules adsorbed on hydrophilic groups decrease the isosteric heat of CO_2 adsorption. The migration of H_2O molecules and the squeeze effect of growing H_2O molecules clusters at higher moisture contents contribute to the increase of the isosteric adsorption heat.

The CO_2/CH_4 adsorption selectivity on kerogen shows no clear relation with maturity, but is greatly affected by the bulk pressure. The adsorption selectivity decreases with the rise of bulk pressure until reaches an equilibrium at high pressure. The effect of moisture content on adsorption selectivity depends on the kerogen model. The selectivity on kerogen IIA, IIC and IID models increase with moisture content, while that on kerogen IIB model decreases with increasing moisture content.

Notes

The authors declare no competing financial interest.

Acknowledgments

This work was supported by the National Natural Science Foundation of China (Grant Nos. 51774298 and 51504265) and the Science Foundation for the Excellent Youth Scholars of China University of Petroleum (Beijing) (Grant No. 2462015YQ0223). Computer time for this study was provided by the HP High Performance Computing Cluster of the State Key Laboratory of Heavy Oil Processing at China University of Petroleum (Beijing).

Appendix A. Supplementary data

Supplementary data associated with this article can be found, in the online version, at http://dx.doi.org/10.1016/j.fuel.2017.09.060.

References

[1] Boyer C, Clark B, Jochen V, Lewis R, Miller CK. Shale gas: a global resource. Oilfield Rev 2011;23:28–39.
[2] Paylor A. The social–economic impact of shale gas extraction: a global perspective. Third World Q 2016:1–16.
[3] White CM, Smith DH, Jones KL, Goodman AL, Jikich SA, LaCount RB, et al. Sequestration of carbon dioxide in coal with enhanced coalbed methane recovery: a review. Energy Fuel 2005;19:659–724.
[4] Chatterjee R, Paul S. Classification of coal seams for coal bed methane exploitation in central part of Jharia coalfield, India – a statistical approach. Fuel 2013;111:20–9.
[5] Vishal V, Singh TN, Ranjith PG. Influence of sorption time in CO_2-ECBM process in Indian coals using coupled numerical simulation. Fuel 2015;139:51–8.
[6] Wang X, Zhai Z, Jin X, Wu S, Li J, Sun L, et al. Molecular simulation of CO_2/CH_4 competitive adsorption in organic matter pores in shale under certain geological conditions. Petrol Explor Dev 2016;43:841–8.
[7] Eshkalak MO, Al-shalabi EW, Sanaei A, Aybar U, Sepehrnoori K. Enhanced gas recovery by CO2 sequestration versus re-fracturing treatment in unconventional shale gas reservoirs. In: Abu Dhabi International Petroleum Exhibition and Conference. Society of Petroleum Engineers; 2014. SPE 172083.
[8] Jiang J, Shao Y, Younis RM. Development of a multi-continuum multi-component model for enhanced gas recovery and CO2 storage in fractured shale gas reservoirs. In: SPE improved oil recovery symposium. Society of Petroleum Engineers; 2014. SPE 169114.
[9] Busch A, Gensterblum Y. CBM and CO_2-ECBM related sorption processes in coal: a review. Int J Coal Geol 2011;87:49–71.
[10] Gensterblum Y, Busch A, Krooss BM. Molecular concept and experimental evidence of competitive adsorption of H_2O, CO_2 and CH_4 on organic material. Fuel 2014;115:581–8.
[11] Mohammad SA, Gasem KAM. Multiphase analysis for high-pressure adsorption of CO_2/water mixtures on wet coals. Energy Fuel 2012;26:3470–80.
[12] Billemont P, Coasne B, De Weireld G. Adsorption of carbon dioxide, methane, and their mixtures in porous carbons: effect of surface chemistry water content, and pore disorder. Langmuir 2013;29:3328–38.
[13] Boult P, Theologou P, Foden J. Capillary seals within the Eromanga basin, Australia: implications for exploration and production. In: Surdam RC, editor. Seals, traps and the petroleum system. AAPG Mem; 1997. p. 143–68.
[14] Hu Y, Devegowda D, Striolo A, Phan A, Ho TA, Civan F, et al. Microscopic dynamics of water and hydrocarbon in shale-kerogen pores of potentially mixed wettability. SPE J 2014;20:112–24.
[15] Herrle JO, Pross J, Friedrich O, Kossler P, Hemleben C. Forcing mechanisms for mid-Cretaceous black shale formation: evidence from the Upper Aptian and Lower Albian of the Vocontian Basin (SE France). Palaeogeogr Palaeocl 2003;190:399–426.
[16] Krooss B, Van Bergen F, Gensterblum Y, Siemons N, Pagnier H, David P. High pressure methane and carbon dioxide adsorption on dry and moisture equilibrated Pennsylvanian coals. Int J Coal Geol 2002;51:69–92.
[17] Clarkson C, Bustin R. Binary gas adsorption/desorption isotherms: effect of moisture and coal composition upon carbon dioxide selectivity over methane. Int J Coal Geol 2000;42:241–71.
[18] Gasparik M, Bertier P, Gensterblum Y, Ghanizadeh A, Krooss BM, Littke R. Geological controls on the methane storage capacity in organic-rich shales. Int J Coal Geol 2014;123:34–51.
[19] Ross DJK, Bustin RM. The importance of shale composition and pore structure upon gas storage potential of shale gas reservoirs. Mar Petrol Geol 2009;26:916–27.
[20] Xu H, Tang D, Liu D, Tang S, Yang F, Chen X, et al. Study on coalbed methane accumulation characteristics and favorable areas in the Binchang area, southwestern Ordos Basin. China. Int J Coal Geol 2012;95:1–11.
[21] Zhang T, Ellis GS, Ruppel SC, Milliken K, Yang R. Effect of organic-matter type and thermal maturity on methane adsorption in shale-gas systems. Org Geochem 2012;47:120–31.
[22] Chalmers GR, Bustin RM. On the effects of petrographic composition on coalbed methane sorption. Int J Coal Geol 2007;69:288–304.
[23] Chalmers GR, Bustin RM. The organic matter distribution and methane capacity of the Lower Cretaceous strata of Northeastern British Columbia. Canada. Int J Coal Geol 2007;70:223–39.
[24] Gensterblum Y, Merkel A, Busch A, Krooss BM. High-pressure CH_4 and CO_2 sorption isotherms as a function of coal maturity and the influence of moisture. Int J Coal Geol 2013;118:45–57.
[25] Hol S, Gensterblum Y, Massarotto P. Sorption and changes in bulk modulus of coal—experimental evidence and governing mechanisms for CBM and ECBM applications. Int J Coal Geol 2014;128:119–33.
[26] Huang L, Ning Z, Wang Q, Qi R, Li J, Zeng Y, et al. Thermodynamic and structural characterization of bulk organic matter in Chinese Silurian shale: experimental and molecular modeling studies. Energy Fuel 2017;31:4851–65.
[27] Zhang J, Clennell MB, Dewhurst DN, Liu K. Combined Monte Carlo and molecular dynamics simulation of methane adsorption on dry and moist coal. Fuel 2014;122:186–97.
[28] Liu X, He X, Qiu N, Yang X, Tian Z, Li M, et al. Molecular simulation of CH_4, CO_2, H_2O and N_2 molecules adsorption on heterogeneous surface models of coal. Appl Surf Sci 2016;389:894–905.
[29] Zhao T, Li X, Zhao H, Li M. Molecular simulation of adsorption and thermodynamic properties on type II kerogen: influence of maturity and moisture content. Fuel 2017;190:198–207.
[30] Loucks RG, Ruppel SC. Mississippian Barnett Shale: lithofacies and depositional setting of a deep-water shale-gas succession in the Fort Worth Basin. Texas. AAPG Bull 2007;91:579–601.
[31] Ungerer P, Collell J, Yiannourakou M. Molecular modeling of the volumetric and thermodynamic properties of kerogen: influence of organic type and maturity. Energy Fuel 2015;29:91–105.
[32] Kelemen SR, Afeworki M, Gorbaty ML, Sansone M, Kwiatek PJ, Walters CC, et al. Direct characterization of kerogen by X-ray and solid-state ^{13}C nuclear magnetic resonance methods. Energy Fuel 2007;21:1548–61.
[33] Jin H, Sonnenberg SA. Characterization for source-rock potential of the Bakken Shales in the Williston basin, North Dakota and South Montana. In: AAPG Annual Convention and Exhibition. AAPG; 2014. p. 37.
[34] Collell J, Ungerer P, Galliero G, Yiannourakou M, Montel F, Pujol M. Molecular simulation of bulk organic matter in Type II shales in the middle of the oil formation window. Energy Fuel 2014;28:7457–66.
[35] Montgomery SL, Jarvie DM, Bowker KA, Pollastro RM. Mississipian Barnett shale, fort worth basin, north-central texas: gas-shale play with multi-million cubic foot potential. AAPG Bull 2005;89:155–75.
[36] Sun H. COMPASS: an ab initio force-field optimized for condensed phase applications overview with details on alkane and benzene compounds. J Phys Chem B 1998;102:7338–64.
[37] Sui H, Yao J. Effect of surface chemistry for CH_4/CO_2 adsorption in kerogen: a molecular simulation study. J Nat Gas Sci Eng 2016;31:738–46.
[38] Ru X, Cheng Z, Song L, Wang H, Li J. Experimental and computational studies on the average molecular structure of Chinese Huadian oil shale kerogen. J Mol Struct 2012;1030:10–8.
[39] Gasparik M, Ghanizadeh A, Gensterblum Y, Krooss BM. "Multi-temperature" method for high-pressure sorption measurements on moist shales. Rev Sci Instrum 2013;84:085116.
[40] Mathias PM, Copeman TW. Extension of the Peng-Robinson equation of state to complex mixtures: evaluation of the various forms of the local composition concept. Fluid Phase Equilibr 1983;13:91–108.
[41] Pan H, Ritter JA, Balbuena PB. Examination of the approximations used in determining the isosteric heat of adsorption from the Clausius-Clapeyron equation. Langmuir 1998;14:6323–7.
[42] Afeefy HY, Liebman JF, Stein SE. NIST chemistry webbook, NIST standard reference database number 69. In: Mallard WG, Linstrom PJ, editors. Gaithersburg MD: national institute of standards and technology. 2000 http://webbook.nist.gov; 2000 [accessed 17.03.01].
[43] Mastalerz M, Schimmelmann A, Lis GP, Drobniak A, Stankiewicz A. Influence of maceral composition on geochemical characteristics of immature shale kerogen: insight from density fraction analysis. Int J Coal Geol 2012;103:60–9.
[44] Okiongbo KS, Aplin AC, Larter SR. Changes in type II kerogen density as a function of maturity: evidence from the Kimmeridge Clay Formation. Energy Fuel 2005;19:2495–9.
[45] Bae JS, Bhatia SK. High-pressure adsorption of methane and carbon dioxide on coal. Energy Fuel 2006;20:2599–607.
[46] Rexer TF, Mathia EJ, Aplin AC, Thomas KM. High-pressure methane adsorption and characterization of pores in Posidonia shales and isolated kerogens. Energy Fuel 2014;28:2886–901.
[47] Hu H. Methane adsorption comparison of different thermal maturity kerogens in shale gas system. Chin J Geochem 2014;33:425–30.
[48] Weniger P, Franců J, Hemza P, Krooss BM. Investigations on the methane and carbon dioxide sorption capacity of coals from the SW Upper Silesian Coal Basin. Czech Republic. Int J Coal Geol 2012;93:23–39.
[49] Wu K, Chen Z, Li X, Dong X. Methane storage in nanoporous material at supercritical temperature over a wide range of pressures. Sci Rep-UK 2016;6:33461.
[50] Lu XC, Li FC, Watson AT. Adsorption measurements in Devonian shales. Fuel 1995;74:599–603.
[51] Loucks RG, Reed RM, Ruppel SC, Jarvie DM. Morphology, genesis and distribution of nanometer-scale pores in siliceous mudstones of the Mississippian Barnett Shale.

J Sediment Res 2009;79:848–61.
[52] Chen J, Xiao X. Evolution of nanoporosity in organic-rich shales during thermal maturation. Fuel 2014;129:173–81.
[53] Wu K, Li X, Wang C, Yu W, Chen Z. Model for surface diffusion of adsorbed gas in nanopores of shale gas reservoirs. Ind Eng Chem Res 2015;54:3225–36.
[54] Wu K, Li X, Guo C, Wang C, Chen Z. A unified model for gas transfer in nanopores of shale-gas reservoirs: coupling pore diffusion and surface diffusion. SPE J 2016;21:1583–611.
[55] Wu K, Chen Z, Li X, Xu J, Li J, Wang K, et al. Flow behavior of gas confined in nanoporous shale at high pressure: real gas effect. Fuel 2017;205:173–83.
[56] Ruppel TC, Grein CT, Bienstock D. Adsorption of methane on dry coal at elevated pressure. Fuel 1974;53:152–62.
[57] Himeno S, Komatsu T, Fujita S. High-pressure adsorption equilibria of methane and carbon dioxide on several activated carbons. J Chem Eng Data 2005;50:369–76.
[58] Lopes FV, Grande CA, Ribeiro AM, Loureiro JM, Evaggelos O, Nikolakis V, et al. Adsorption of H_2, CO_2, CH_4, CO, N_2 and H_2O in activated carbon and zeolite for hydrogen production. Sep Sci Technol 2009;44:1045–73.
[59] Zhang J, Liu K, Clennell M, Dewhurst D, Pervukhina M. Molecular simulation of CO_2–CH_4 competitive adsorption and induced coal swelling. Fuel 2015;160:309–17.
[60] Brochard L, Vandamme M, Pelenq RJM, Fen-Chong T. Adsorption-induced deformation of microporous materials: coal swelling induced by CO_2–CH_4 competitive adsorption. Langmuir 2012;28:2659–70.